



<b>Title</b>	Reconciliation of contrasting theories for fracture spacing in layered rocks
<b>Authors(s)</b>	Schöpfer, Martin P. J., Arslan, Arzu, Walsh, John J., Childs, Conrad
<b>Publication date</b>	2011-04
<b>Publication information</b>	Schöpfer, Martin P. J., Arzu Arslan, John J. Walsh, and Conrad Childs. "Reconciliation of Contrasting Theories for Fracture Spacing in Layered Rocks." Elsevier, April 2011. <a href="https://doi.org/10.1016/j.jsg.2011.01.008">https://doi.org/10.1016/j.jsg.2011.01.008</a> .
<b>Publisher</b>	Elsevier
<b>Item record/more information</b>	<a href="http://hdl.handle.net/10197/3026">http://hdl.handle.net/10197/3026</a>
<b>Publisher's statement</b>	This is the author's version of a work that was accepted for publication in Journal of Structural Geology. Changes resulting from the publishing process, such as peer review, editing, corrections, structural formatting, and other quality control mechanisms may not be reflected in this document. Changes may have been made to this work since it was submitted for publication. A definitive version was subsequently published in Journal of Structural Geology Volume 33, Issue 4, April 2011, Pages 551-565 DOI#:10.1016/j.jsg.2011.01.008.
<b>Publisher's version (DOI)</b>	<a href="https://doi.org/10.1016/j.jsg.2011.01.008">10.1016/j.jsg.2011.01.008</a>
<b>Notes</b>	Associated movies require QuickTime to view

Downloaded 2025-12-04 22:26:51

The UCD community has made this article openly available. Please share how this access benefits you. Your story matters! (@ucd\_oa)



© Some rights reserved. For more information

# Reconciliation of contrasting theories for fracture spacing in layered rocks

Martin P.J. Schöpfer\*, Arzu Arslan†, John J. Walsh, Conrad Childs

*Fault Analysis Group, UCD School of Geological Sciences,  
University College Dublin, Belfield, Dublin 4, Ireland.*

## Abstract

Natural and man-made brittle layers embedded in a weaker matrix and subjected to layer-parallel extension typically develop an array of opening-mode fractures with a remarkably regular spacing. This spacing often scales with layer thickness, and it decreases as extension increases until fracture saturation is reached. Existing analytical one-dimensional (1-D) 'full-slip' models which assume that interfacial slip occurs over the entire length of the fracture-bound blocks predict that the ratio of fracture spacing to layer thickness at saturation is proportional to the ratio of layer tensile to interface shear strength ( $T/\tau$ ). Using 2-D discontinuum mechanical models run for conditions appropriate to layered rocks we show that the validity and consequent applicability of these 1-D models depends on  $T/\tau$ . High  $T/\tau$  ratios (*ca.*  $> 3.0$ ) promote interfacial slip and yield results that, in terms of fracturing and interfacial slip evolution, provide a good fit to a 1-D shear lag model, which, in the limit, becomes the 'full-slip' model. At lower  $T/\tau$  ratios, however, interfacial slip is suppressed and the heterogeneous 2-D stress distribution within fracture-bound blocks controls further fracture nucleation. Our models suggest that 1-D approximations for predicting the spacing of fractures in layered materials are erroneous for low  $T/\tau$  ratios.

*Keywords:* Fracture spacing; Rock joints; Shear lag model; Distinct Element Method;

---

\*Corresponding author. E-mail: martin@fag.ucd.ie Tel: +353 1 716 2611 Fax: +353 1 716 2607

†Present address: Center for Marine Environmental Sciences, Leobener Strasse, D-28359 Bremen, Germany.

# 1 Introduction

Opening-mode fractures are extremely common phenomena in natural and man-made materials. In geosciences they are referred to as joints (Mandl, 2005) and in engineering they are termed cracks (Nairn, 2000). In mechanically layered materials, such as sedimentary rock sequences or laminates, these fractures typically form perpendicular to the layer boundaries and are often best, or exclusively, developed in the stiffer and more brittle layers (Fig. 1a), although under some circumstances fractures may first form in the weaker beds (Bourne, 2003). Studies of these fractures in layered rocks (Ladeira and Price, 1981, Huang and Angelier, 1989, Narr and Suppe, 1991, Ji and Saruwatari, 1998, Ji et al., 1998, Gillespie et al., 2001, Iyer and Podladchikov, 2009), physical experiments (Garrett and Bailey, 1977, Mandal et al., 1994, Wu and Pollard, 1995) and numerical models (Tang et al., 2008) have revealed that fracture spacing increases with layer thickness. A wide variety of mechanisms have been suggested for the origin and scaling relations of layer-confined opening-mode fractures (Bourne, 2003, Mandl, 2005). In the present study, we focus on one of the most commonly used boundary conditions for investigating the mechanics of opening-mode fractures in layered materials: fracturing due to layer-parallel extension under constant layer normal stress. For this case, experimental work has revealed that fracture spacing decreases approximately as the inverse of the applied layer-parallel strain (Manders et al., 1983, Parvizi and Bailey, 1978). This is because new fractures form in-between existing fractures, a process referred to as *sequential infilling* (Bai et al., 2000, Bai and Pollard, 2000b). Eventually no new fractures form, irrespective of any further increase in applied strain, a condition called *fracture saturation* (Wu and Pollard, 1995, Bai et al., 2000, Bai and Pollard, 2000b, Dharani et al., 2003).

The earliest and most commonly invoked mechanical explanation for fracture saturation is that the fracture spacing reaches a critical value (relative to the layer thickness,  $t$ ) at which maximum tensile stresses within the fracture bound blocks are too low to yield further fracture. This explanation is based on the concept of frictional coupling between the fractured layer and the ambient material or 'matrix' (Fig. 1b). The layer/matrix

interface has a frictional strength  $\tau$  given by the Coulomb limit stress  $\sigma_n\mu$ , where  $\sigma_n$  is the interfacial normal stress and  $\mu$  is the interfacial friction coefficient (Mandl, 2005). The static balance of mechanical forces requires that a constant interfacial shear stress,  $\tau$ , is balanced by a constant layer-parallel *average* stress gradient,  $d\sigma_x/dx$  (Fig. 1b). If slip occurs over the entire length of a fracture-bound block (*full-slip* conditions), the layer-parallel normal stress ( $\sigma_x$ ) distribution between two traction free fractures is triangular, with the maximum tensile stress occurring in the block centre (Fig. 1b). This central maximum tensile stress is, however, limited by the tensile strength of the layer,  $T$ . The *critical fracture spacing* ( $s_c$ ) is therefore defined as the spacing below which the maximum tensile stress can not reach the layer strength, i.e.  $s_c = Tt/\tau$  (Fig. 1b).

The above equation is known as Price’s model in the geologic literature (Price, 1966, Mandl, 2005) and as the Kelly-Tyson equation in material sciences (Kelly and Tyson, 1965, Tripathi and Jones, 1998). For laminates and fibre composites, it is widely applied to estimate interfacial shear strength from fragment length measurements (Tripathi and Jones, 1998). This *full-slip* model is the most commonly applied end-member of a suite of models referred to as *shear lag models* (Cox, 1952, Hobbs, 1967, Piggott, 1978, Lloyd et al., 1982, Berthelot et al., 1996, Ji and Saruwatari, 1998, Ji et al., 1998, Berthelot, 2003, Jain et al., 2007). Different shear lag models vary in the assumed modes of transfer of tensile stress across the layer/matrix interface, e.g. the full-slip model is the limit solution (at infinite layer extension;  $e \rightarrow \infty$ ) for a cohesionless frictional interface. Although differing in detail, shear lag models all predict that sequential infill fractures should form midway between existing fractures, such that the range of fracture spacing at a particular strain varies by a factor of two, i.e.  $0.5s_c < s < s_c$ . The average fracture spacing is hence given by  $\bar{s} = 0.75s_c$ , an expression sometimes referred to as the Ohsawa *et al.* equation (Ohsawa et al., 1978, Tripathi and Jones, 1998).

Despite their successful application in material science (Berthelot et al., 1996, Berthelot, 2003), the limitations of shear lag models are manifest in a variety of ways. For example, whilst physical experiments without any clear evidence for interfacial slip can

attain fracture saturation (Garrett and Bailey, 1977), shear lag models with inhibited interfacial slip ( $\tau \rightarrow \infty$ ) predict fracturing *ad infinitum* (Bai et al., 2000). In addition, they are unable to account for fracture clustering in 'corridors' (Olson, 2004) or 'crack families' (Groves et al., 1987) and for the formation of splay, i.e. branch, fractures. This is because the feature common to all shear lag models is that they are based on stresses averaged over the thickness of the layer, i.e. they are effectively 1-D treatments. Consideration of layer-normal  $\sigma_{xx}$  variations and the near crack tip stress field on fracturing is thus absent.

### Figure 1

An alternative explanation for fracture saturation in the absence of interfacial slip is that segment-bounding fractures become sufficiently closely spaced such that a layer-parallel compressive normal stress arising between the existing fractures prevents the insertion of new fractures (Altus and Ishai, 1986). This is referred to as *compressive stress criterion* (CSC; Dharani et al., 2003) or *stress-transition theory* (Bai et al., 2000, Bai and Pollard, 2000b). The CSC is based on 2-D numerical (Bai et al., 2000, Bai and Pollard, 2000b, Korach and Keer, 2002, Li and Yang, 2007) and analytical (Schoepner and Pagano, 1999, Adda-Bedia and Amar, 2001) modelling of the stress distribution between two predefined fractures. For a fracture spacing to layer thickness ratio of approximately one, this modelling reveals that a region of compressive layer-parallel normal stress  $\sigma_{xx}$  develops right across the central area of the fracture-bound block (Bai et al., 2000, Bai and Pollard, 2000b, Fig. 1c). This central compression belt will inhibit further fracturing, although numerical analysis indicates that tensile stresses adjacent to the interface (Fig. 1c) may be sufficient to cause propagation of vertical fractures across this belt from interface-flaws mid-way between the two existing fractures (Bai and Pollard, 2000a). Fracture saturation occurs when a limiting fracture spacing to thickness ratio is reached, at which fractures can not propagate across the compressive belt. For identical layer and matrix elastic properties, this limit is  $s/t = 0.546$ , such that  $s_{min}/t$  for a fracture set at complete infilling would be 0.273 (Bai and Pollard, 2000a). This predicted range is referred to as the *2-D infill criterion*.

Whilst the CSC theory provides a rationale for fracture saturation without interfacial slip, unlike the shear lag models, it is limited because it does not include such slip. Experimental studies on fibres (Huang and Young, 1995, van den Heuvel et al., 1997, Tripathi and Jones, 1998) and laminates (Berthelot, 2003), for example, have shown that during extension interfacial slip, or, in the presence of cohesion, interface debonding, occurs. Analysis of plume lines on joint faces also suggests that interfacial, e.g. bedding parallel, slip or matrix yielding must sometimes occur during joint growth (Savalli and Engelder, 2005). Moreover, and importantly, the CSC theory does not account for observations of fracture saturation at  $s/t$  ratios in excess of one.

The above considerations suggest that a fuller explanation of fracture scaling relationships for the wide range of naturally occurring and man-made interface properties requires a more complete model definition, ideally one which incorporates behaviours explained by both theories illustrated in Fig. 1. Here we describe discontinuum numerical models that explicitly replicate fracturing of a layer in response to layer-parallel extension and to 2-D stress distributions within fracture blocks. We consider a range of layer/matrix interface properties and compare our model results with those of shear lag and CSC theories.

## 2 Methods

### 2.1 Model geometry and boundary conditions

In our discontinuum models the layer and matrix are represented as an assemblage of bonded circular particles (Fig. 2; Potyondy and Cundall, 2004). The bonds between particles comprising the central layer fail if their strength is exceeded and the linkage of those broken bonds leads to the formation of fractures. The particles and bonds do not represent sand grains and cement, respectively; they merely provide a numerical material that mimics the mechanical response of brittle materials (see Appendix A for details). A drawback of discretisations using randomly placed particles is that the simulated fractures are jagged, whereas rock joints are often remarkably smooth. This aesthetic shortcoming will in the future be resolved by the generation of progressively higher resolution models,

with smaller particle sizes. Discontinuum models with regular (e.g. cubic) particle packing also permit the formation of straight fractures, but would however inhibit the formation of non-planar fractures, which, as shown later, are an important feature in some of our models.

## Figure 2

In all our models the first fracture forms wherever the layer is weakest (discontinuum models have heterogeneous strength distributions; see Appendix A) when the average tensile stress within the layer reaches  $\sim 6.5$  MPa (see Fig. A1), a tensile strength typical for sedimentary rock (e.g. limestone, sandstone; Lockner, 1995). Failure within the matrix is prevented so that matrix yielding and fracturing does not affect fracture within the central layer. Layer-matrix interface geometries and frictional properties are represented through a so-called 'smooth-joint' contact model (Itasca Consulting Group, Inc., 2008, Mas Ivars et al., 2008) that implicitly replaces the irregular geometry of an interface between domains within a particle assemblage with a planar discontinuity (Fig. 2). After uniaxial confinement this three-layer model is extended horizontally with a velocity low enough to assure quasi-static conditions, while maintaining a constant vertical stress of -5 MPa which, under lithostatic conditions and for an overburden density of  $2500 \text{ kg/m}^3$ , is equivalent to a depth of  $\sim 200$  m (Fig. 2); our results are however applicable to a broader range of confining pressure and tensile strength because the controlling factor is  $T/\tau$  (see below). Further details of the modelling are given in Appendix A.

We present results from four models with non-cohesive interfaces with friction coefficients  $\mu$  of 0.2, 0.3, 0.5 and 0.8 and one model with a welded interface. All models attain a finite strain of 0.008 and fracture saturation. The friction coefficients used in this study cover the wide range reported by Byerlee (1978) for confining pressures of  $< 5$  MPa, at which the large variation in friction is due to variation in surface roughness. Although experimental constraints on the frictional properties of lithological interfaces (e.g. bedding planes) are very sparse, we consider that the broad range, and in particular the lower values, used in this study are appropriate. A range of interfacial shear strengths was

achieved by varying the interfacial friction coefficient, rather than the confining pressure, because the latter would also cause variations in both elastic properties and strength due to their pressure dependence (e.g. Schöpfer et al., 2009). The role of the interfacial friction in our models is simply to limit the interfacial shear stress; whether this is achieved in a natural system by interfacial slip and/or plasticity of the matrix layers depends on a wide range of extrinsic and intrinsic parameters. In fact, if the interfacial shear strength is greater than the shear strength of the matrix then the strength of the (plastic) matrix in shear is the controlling factor in determining fracture spacing (Kelly and Tyson, 1965).

## 2.2 Graphical representation

The model evolutions and their differences can be explored by generating the three types of plot presented in Fig. 3 for different models at different stages of their evolution. Animations of these plots of the five different models presented in this paper are provided as an electronic supplement. Each of these three forms of output are outlined below:

(i) Broken bonds and interface slip diagram: Shows the locations of sliding 'smooth-joint' contacts and broken bonds. If sliding occurs on a 'smooth-joint' contact, it is drawn as a horizontal line at the contact location, with a length equal to the area of the 'smooth-joint'. A sliding contact is defined as a contact where  $|\mathbf{F}_s| > 0.99\mathbf{F}_n\mu$ , where  $\mathbf{F}_n$  and  $\mathbf{F}_s$  are the contact normal (+ve) and shear force, respectively. Each broken bond, or 'crack', is drawn as a black line (Figs. 3 and 4) half-way between the two initially bonded particles, with a length equal to the average diameter of the two particles and perpendicular to a line joining the particle centres.

(ii) Horizontal normal stress plot: Shows the average horizontal normal stress ( $\sigma_x$ ) distribution within the central layer (as defined by Eq. C.1). The stress is normalised by the minimum layer tensile strength  $T_{min}$ , defined as the stress at which the first fracture forms (Fig. A1). If the layer strength and horizontal stress ( $\sigma_{xx}$ ) distributions were homogeneous, then subsequent fracturing would occur at the same stress level. However, the particulate nature of the model makes the material intrinsically



heterogeneous, so that the average horizontal normal stress can exceed  $T_{min}$ , i.e. 1.0 in the graph. Most importantly, if the heterogeneous  $\sigma_{xx}$  distribution controls fracture, as in the high interfacial strength models, then fracture can occur at stress levels which are significantly lower than the *average* layer strength.

- (iii) Interfacial shear stress plot: Shows the interfacial shear stress distributions, expressed as the ratio of shear to normal stress,  $\tau_{xy}/\sigma_{yy}$ , for each 'smooth-joint' contact, with clockwise shear couples taken to be positive (Fig. 3). In case of the cohesionless, frictional interface models the maximum value of this ratio is limited by the friction coefficient,  $\mu$ . We therefore plot  $\tau_{xy}/\sigma_{yy}/\mu$  (i.e.  $\tau_{xy}/(\mu\sigma_{yy})$ ), so that the data plotted range from -1.0 to 1.0. Values of -1.0 or 1.0 hence indicate that anti-clockwise and clockwise interfacial slip occurs, respectively.

### Figure 3

## 3 Results

The fracture spacing and interfacial slip evolution of the discontinuum models with various interfacial friction coefficients are shown in Figs. 4 and 5. The discontinuum model results are compared with predictions based on a shear-lag model with interfacial slip which, in the limit, yields a finite fracture spacing equivalent to the full-slip model (see Appendix B and Appendix C).

### Figure 4 & 5

#### 3.1 Low interfacial friction models ( $\mu = 0.2$ and $\mu = 0.3$ )

For  $\mu = 0.2$  and  $\mu = 0.3$  (Fig. 5) there is good agreement between discontinuum and shear-lag model predictions for the evolution of fracture spacing and reasonable agreement for the proportion of slip (which is defined as the ratio of the sum of sliding 'smooth-joint' contact areas to the sum of all 'smooth-joint' contact areas). This similarity of results

occurs because the dominant process in both models is mid-point fracture (Figs. 3 and 4).

The stress evolution in the low friction models is in close agreement with theoretical considerations (Fig. 3; see also Appendix B). Once a fracture forms the average layer-parallel normal stress at this location drops to zero and interfacial shear stresses develop adjacent to the fracture. If the interfacial shear stress exceeds the shear strength interfacial slip commences. In each fracture-bound block the shear sense is symmetric across a horizontal mirror plane through the centre of the layer and a vertical mirror plane through the centre of the block (Fig. 3a). The length of the slip regions decreases with increasing interfacial shear strength (see first row in Fig. 4) and the vertical shear stress gradient is balanced by a horizontal normal stress gradient, which is constant in the slip regions. Fracture saturation in the low friction models occurs when slip occurs along the entire interface as predicted by the *full-slip* model (compare Figs. 1b and 3b)

### 3.2 High interfacial friction models ( $\mu = 0.5$ and $\mu = 0.8$ )

For  $\mu = 0.5$  and  $\mu = 0.8$  (Fig. 5) there is poor agreement between discontinuum and shear-lag model predictions (the deviation from the shear lag prediction is greater for the higher friction model). The discontinuum modelling yields a much larger range of fracture spacings during system evolution than the factor of 2 variation predicted by the shear lag model and it produces a much lower average spacing at saturation.

## Figure 6

Both of these discrepancies arise because 2-D heterogeneous stress distributions within fracture-bound blocks, which are unaccounted for in the 1-D shear lag model, exert important controls on fracturing in the discontinuum models with high interface frictions. Fracture saturation in the  $\mu = 0.8$  discontinuum model arises largely by the same process as described for the *2-D infill criterion* (compare Figs. 1c and 6b), i.e. infill fractures can not propagate across a belt of compressive stress at the centre of a fracture block once a

critical  $s/t$  ratio is achieved (this critical  $s/t$  is  $\ll 1.0$  in our models). However, the wider range of fracture spacing than the factor of 2 variation prediction by mid-point fracture throughout the evolution of the  $\mu = 0.5$  and  $\mu = 0.8$  discontinuum model is due to the formation of new fractures close to existing fractures in blocks with  $s/t \gg 1$  (Fig. 4). Neither the shear lag nor CSC theories predict these new fractures, but their formation is consistent with the commonly observed clustering of fractures in real layered materials. In our models, the new fractures nucleate at interfaces and either propagate across the layer to form through-going fractures or link with existing fractures to form splays/branches (Fig. 6). They form when the maximum principal (least compressive) stress near the interface is located in close proximity to the existing fractures (Groves et al., 1987, Hu et al., 1993), rather than mid-way between them as predicted by 1-D analyses. The new fractures propagate along curved principal stress trajectories that are convex towards the earlier fracture (Fig. 6a). Such curved fractures are indeed observed in some laminates (Groves et al., 1987, Hu et al., 1993).

### 3.3 Reconciliation of fracture saturation theories

Fracture spacings at saturation as predicted by the *1-D full-slip model* (Price's or Kelly-Tyson equation), the *compressive stress criterion* (CSC) and the *2-D infill criterion*, and as observed in discontinuum modelling, are compared in Fig. 7. There is good agreement between the full-slip model and the discontinuum models at friction coefficients of  $\mu < 0.4$  (Fig 7a). At higher friction coefficients, however, the discontinuum modelling predicts a wider range of fracture spacing than the full-slip model and a lower average spacing. Instead, the discontinuum model spacings here overlap with predictions of the alternative 2D infill criterion, which is thus shown to become more appropriate as welded interface conditions are approached. Moreover, and in contrast to the unrealistic zero spacing predicted by the full-slip model, the discontinuum model predicts spacings at saturation in close agreement with the 2-D infill criterion at  $T/\tau$  ratios approaching zero (i.e. a welded interface; Fig 7b).

We presume that the  $T/\tau$  value limiting the validity of 1-D approximations will be greatly controlled by the size of existing flaws and may therefore vary widely as a function of material heterogeneity (Tang et al., 2008).

## Figure 7

## 4 Discussion

Distinct Element Method modelling of the fracturing of a brittle layer embedded in a weaker matrix provides a rationale for the wide range of fracture characteristics observed in nature (e.g. Sagy and Reches, 2006). With increasing layer parallel extension, new fractures form in-between existing fractures, a process referred to as sequential infilling, until no new fractures form when fracture saturation is reached. The resulting fracture distributions are often scale-dependent, with approximately regular fracture spacing which scales with layer thickness, features which are typical of natural and man-made fracture systems. Fracture spacing at saturation does, however, vary with the layer tensile to interface shear strength ratio ( $T/\tau$ ) and is therefore not, as previous work has suggested, an indicator of fracture system maturity or saturation (all models shown in the lowest row in Fig. 4 are saturated). Conclusions about fracture saturation arising from numerical models with predefined fractures that do not explicitly permit fracture nucleation, propagation and associated interfacial slip (Bai and Pollard, 2000b) can, therefore, be misleading. Variations in layer tensile to interface shear strength ratios ( $T/\tau$ ) can also lead to changes in both fracture spacing populations and fracture geometries. At high  $T/\tau$  ratios fractures are straight, fracture spacings are quasi-periodic and fracture spacing to layer thickness ratios at saturation range down to *ca.* 2 (Fig. 7), values which are typical of many fracture systems. At lower  $T/\tau$ , by contrast, fractures become more curved and branched, clustered fracture patterns emerge and fracture spacing to layer thickness ratios at saturation are often less than 1. Whilst existing analytical one-dimensional (1-D) full-slip models are in good agreement with higher  $T/\tau$  models, at lower  $T/\tau$  interfacial slip is suppressed and 2-D stress distributions within fracture-bound blocks controls fur-

ther fracture nucleation. Detailed analysis of the precise nature of fracture distributions and shape, and how they change with mechanical parameters, such as  $T/\tau$  ratio and layer properties, is beyond the scope of this study but could have significant scientific and practical benefits. Our modelling shows, for example, that fracture branching and clustering is not necessarily an indicator of either dynamic crack propagation (Sagy and Reches, 2006) or sub-critical crack growth (Olson, 2004). Branches and curved fractures in our models nucleate at the layer interface and propagate towards existing straight fractures, a scenario which was envisaged, but not investigated, in a study on fracture stepping across interfaces (Cooke and Underwood, 2001). Perhaps the analysis of plume lines on natural joint faces may reveal whether branched fracture geometries arise from either fracture bifurcation or fracture linkage.

Our models reproduce many aspects of the geometry and evolution of fracture patterns in single layers and also provide a basis for considering the potential impact of some other factors:

- (i) **Confining pressure and strength:** In this study we have explored the impact of interfacial friction coefficient on fracturing in a three-layer system under a constant confining pressure (Fig. 7a), defined by a constant layer-normal stress of -5 MPa which is equivalent to  $\sim 200$  m depth for lithostatic conditions and an overburden density of  $2500 \text{ kg/m}^3$ . In a horizontally layered sequence the interfacial shear strength  $\tau$  of cohesionless interfaces is the product of the vertical stress  $\sigma_v$  and the friction coefficient  $\mu$ , such that  $|\tau| = \sigma_v \mu$ . We expect, therefore, that similar relations to those shown in Fig. 7 will arise for constant  $\mu$  and for variable  $\sigma_v$ , which under lithostatic conditions is given by  $\gamma h$  (where  $\gamma$  is the specific weight of a rock column extending down to a depth of  $h$ ). If pore water is present then the *effective* vertical stress is given by  $\sigma'_v = \sigma_v(1 - \lambda_v)$ , where  $\lambda_v$  is the ratio of pore fluid pressure  $p_f$  to vertical stress  $\sigma_v$  (Sibson, 1998, Mandl, 2005). Under normal hydrostatic conditions ( $\lambda_v = 0.4$ ) an effective vertical stress of -5 MPa would hence be equivalent to a depth of 340 m. The above relationships mean that for a constant interfacial friction

coefficient and layer tensile strength, a decrease in fracture spacing at saturation is expected with increasing depth; the actual depth depends on overburden density and pore pressure (Fig. 8). At certain depths, however, confining pressure inhibits the formation of opening-mode fractures and there is a transition to shear fracturing (Sibson, 1998, Ramsey and Chester, 2004, Schöpfer et al., 2007). By the same token, in a sequence which is deformed at a constant confining pressure a systematic decrease of fracture spacing will accompany a decrease in layer strength, until at a certain strength a transition to shear failure will occur (Fig. 8).

(ii) **Interface cohesion:** The layer/matrix interfaces in our models are cohesionless, a simplification which cannot always be justified in a natural system. We expect that cohesion will decrease fracture spacing and that Price’s full-slip model could potentially overestimate saturation fracture spacing. Indeed, our ongoing discontinuum modelling of cohesive interfaces suggests that the layer-parallel normal stress profiles (Fig. 3ii) exhibit a central convex upwards region (corresponding to the intact interface) which at the cusps exhibit a steeper slope than in the slip region (Piggott, 1997). The tensile stress within this central region can be higher than for a cohesionless interface and can hence cause further fracturing.

(iii) **Elastic properties and layer/matrix thicknesses:** Our modelling verifies Price’s *full-slip* model for cohesionless interfaces and high layer tensile to interface shear strength ratios ( $T/\tau$ ). Because Price’s model is solely based on a balance of mechanical forces under interfacial full-slip conditions, elastic properties and matrix thicknesses have no impact on fracture spacing at saturation (the detailed evolution of fracture spacing is theoretically dependent on these properties). The 2-D stress distribution within fracture bound blocks under no-slip conditions is, however, sensitive to the elastic properties (Bai and Pollard, 2000b) and layer/matrix thicknesses. Consequently we expect slightly different results at low  $T/\tau$  ratios for models with different elastic properties and thickness ratios, though future work is required to

verify the nature of these dependencies.

- (iv) **Multilayers:** Our models are for simple three-layer systems rather than the more complex multilayered systems often found in nature. Geological studies suggest, for example, that fracture pattern scaling may be hierarchical perhaps reflecting the stacking patterns and mechanical amalgamation of fractured layers (e.g. Gillespie et al., 2001). Experimental work on composite materials has shown that a fracture in one layer can raise the stress in the adjacent layers and hence can lead to fracture alignment, in particular when the matrix layers are thin (van den Heuvel et al., 1997). The fracture-related interactions between different mechanical layers in a layered sequence and their impact on fracture systematics could be the subject of future studies using the same basic modelling approach described in this paper.

## Figure 8

## 5 Conclusions

Our discontinuum models of fracture of single layers with various interfacial shear strength suggests the following principal conclusions:

1. The validity and consequent applicability of Price's *full-slip* model, and similar 1-D approximations, depends on the ratio of layer tensile strength to interface shear strength ( $T/\tau$ ).
  - (a) High  $T/\tau$  ratios (*ca.*  $> 3.0$  in our models) promote interfacial slip and yield results that provide a good fit to a 1-D shear lag model.
  - (b) At lower strength ratios interfacial slip is suppressed and the heterogeneous 2-D stress distribution within fracture-bound blocks controls further fracture nucleation (curved fractures, infill fractures).
2. In systems with high  $T/\tau$  ratios the range of fracture spacing varies by a factor of two because the dominant fracture mode is *mid-point fracturing*. Systems with lower

strength ratios exhibit a wider range of fracture spacing with a bimodal spacing distribution due to the formation of curved fractures close to existing fractures.

3. The *compressive stress criterion* (CSC), or *stress transition theory*, appears not to be valid since further infill fractures nucleate at the layer/matrix interfaces and propagate through the centre of the fracture-bound blocks, hence the *2-D infill criterion* is more appropriate.
4. Fracture saturation spacing decreases non-linearly with increasing interface shear strength and therefore decreases with increasing effective layer normal stress, e.g. overburden pressure.
5. In a layered sequence that permits interfacial slip, fracture spacing is not an indicator of fracture system maturity, or saturation, i.e. a fracture spacing to layer thickness ratio of  $\gg 1$  does not imply that the system is unsaturated.

## Acknowledgements

We thank C. Bean, M. Gilchrist, E. Holohan, T. Manzocchi and G. O'Brien (UCD), and T. Engelder (Penn State) for fruitful discussions. The staff of Itasca, in particular P. Cundall, D. Mas Ivars, M. Pierce and D. Potyondy, is acknowledged for valuable suggestions and for providing additional PFC-2D licenses and software training. Thorough reviews by G. Lloyd (Leeds) and D. Pollard (Stanford) are appreciated. This work was funded by Science Foundation Ireland (SFI) research grants 07/RFP/GEOF340 and 08/RFP/GEO1170.



370 **Notation**

$d$	thickness of matrix layers
$E_f$	Young's modulus of fractured layer
$e$	model strain
$e_m$	matrix strain
$e_p$	pre-strain
$g$	average layer-parallel normal stress gradient
$G_m$	shear modulus of matrix
$L$	half-length of fracture-bound block
$L_c$	critical half-length of fracture-bound block
$m$	fraction of no-slip region
$s$	fracture spacing
$t$	thickness of fractured layer
$T$	tensile strength of fractured layer

371

$\alpha$	fraction of area occupied by particles
$\beta$	load transfer parameter
$\mu$	interfacial friction coefficient
$\sigma_p$	pre-stress
$\sigma_x$	average layer-parallel normal stress in fractured layer
$\sigma_{xx}$	layer-parallel normal stress component
$\sigma_{xx}^p$	layer-parallel normal stress component of particles
$\sigma_y$	interfacial normal stress
$\tau$	interfacial shear strength
$\tau_x$	interfacial shear stress

## Appendix A Distinct Element Method

### A.1 Particle properties and boundary conditions

The modelling in this study was performed with the PFC-2D software, which implements the Distinct Element Method (DEM). The models were generated using the sample generation procedure detailed in Potyondy and Cundall (2004). The model boundaries are rigid and frictionless. Particles have a uniform size distribution with a particle size range of 0.0015-0.0025 m and comprise a model area fraction of 0.84. All particle contacts have a contact friction coefficient of 0.5 and are assigned a linear contact model. Particle and bond Young's moduli are equal and are 50.00 and 16.67 GPa within the central layer and matrix, respectively. The particle and bond normal to shear stiffness ratio is 2.5 and the modulus-stiffness scaling relations given in Potyondy and Cundall (2004) are applied. Bonds between particles comprising the matrix have infinite bond strength and bonds within the central layer have a tensile and shear strength of 20 MPa. Despite the constant bond strength parameters, variations in local strength arise from changes in local particle packing, with the resulting heterogeneity being an intrinsic feature of bonded particle models. Accelerating motion is damped with a damping constant of 0.7. After a bonded-particle model is generated with an initial isotropic stress of -0.1 MPa, contacts between particles comprising the layer and matrix are assigned a 'smooth-joint' model, which simulates the behaviour of a horizontal interface regardless of the local contact plane orientations along the interface (Fig. 2). The area of each 'smooth-joint' contact is scaled so that the sum of all contact areas is equal to the total length of the interface represented as 'smooth-joints'. The model is then confined vertically, with zero interfacial friction, until the desired confining pressure of -5 MPa is reached. If during confinement or later extension a new contact between a matrix and layer particle is formed (e.g. due to shear displacement) this contact is assigned a 'smooth-joint' model, otherwise spurious contact forces would develop due to asperity lockup. After confinement particles touching the lateral boundaries and their neighbours (black particles in Fig. 2) are assigned a hor-

horizontal outward finite velocity of 0.005 m/s (this finite velocity is reached incrementally in order to minimize dynamic effects) and the model specific 'smooth joint' friction and cohesion are assigned. During extension the vertical confinement is maintained using a servo-algorithm.

## Figure A1

### A.2 Mechanical properties of central layer

Average stresses and strains are measured in three circular regions within the central layer using so-called measurement circles (Itasca Consulting Group, Inc., 2008, Potyondy and Cundall, 2004, see inset in Fig. A1). These average stress data are used for determining the macroscopic mechanical properties (modulus, strength) of the central layer. A plot of average layer-parallel stress within these three measurement circles vs. model strain is shown in Fig. A1. For each model, various parameters were determined using the average of the three measurement circle data, and are summarised in Table A1. Initial uniaxial confinement ( $\sigma_y = -5$  MPa) leads to a horizontal pre-stress  $\sigma_p$  due to Poisson's effect (Poisson's ratio under uniaxial loading and plane-stress conditions is  $\nu = \sigma_p/\sigma_y$ ). Model extension causes an increase in horizontal stress until the first fracture develops. The stress level at which the first fracture develops is interpreted to be the minimum layer tensile strength,  $T_{min}$ , under *homogeneous* stress conditions. The fact that the three curves in Fig. A1 are basically identical until fracturing commences indicates that the stress distribution is initially homogeneous. However, the stress-strain curves change their slopes when  $\sigma_x$  becomes tensile, at a pre-strain  $e_p$ , and hence suggest that Young's modulus depends on the sign of the least compressive stress. Young's modulus, under plane-stress conditions, is the slope of the stress-strain curve,  $\Delta\sigma_x/\Delta e_x$ . When all stresses are compressive, the secant Young's modulus is  $E_p = -\sigma_p/e_p$ , whereas when the least compressive stress is tensile Young's modulus is  $E_f = T_{min}/\Delta e$ , where  $\Delta e = e - e_p$ . We use the latter modulus for fitting the shear lag model.

## Table A1

It is important to note that formulation of the shear lag model described in Appendix B predicts zero stress for zero matrix strain. In the fitting procedure given in Appendix C we therefore use  $e_m = e - e_p$ , i.e. the pre-strain is subtracted from the model strain. In the plots shown in Fig. 5, this pre-strain is then added to the shear lag prediction.

## Appendix B Shear lag model

### B.1 Geometry and boundary conditions

Consider a periodically layered sequence of alternating 'soft' (so-called 'matrix') and 'strong' materials which are fractured (Fig. B1a). The matrix layers have a thickness  $d$  and a shear modulus  $G_m$ . The fractured layers have a thickness  $t$  and a Young's modulus  $E_f$ . The fractures are equally-spaced with a spacing  $s$ , but because of the symmetry of the problem we use the half-length  $L$  throughout this Appendix.

### Figure B1

The boundary conditions acting on a 'unit-cell' are schematically illustrated in Fig. B1a. A layer-parallel axial stress is induced in the system by displacing the ends of the matrix layers, while keeping the fractures traction free. The average strain in the matrix is  $e_m$ . This boundary condition leads to a layer-parallel tensile stress within the fracture-bound block, with a maximum in the centre. An interfacial shear stress also develops, as indicated with half-arrows in Fig. B1a, which decreases in a vertical direction and becomes zero along horizontal lines centred in the matrix layers. Because the shear stresses acting along one interface are opposite in sign on either side of the fracture-bound block (Fig. B1a), the shear stress along a vertical line centred in the block must vanish.

To approximate this 2-D problem, stresses and strains are interpreted in an average, rather than local sense, so that the shear lag model is a 1-D approximation. The *average* horizontal, or layer-parallel, normal stress  $\sigma_x$  within a layer of thickness  $t$  centred at  $y_0$  is defined as (e.g. Iyer and Podladchikov, 2009)

$$\sigma_x(x) = \frac{1}{t} \int_{y_0-t/2}^{y_0+t/2} \sigma_{xx}(x, y) \, dy \quad (\text{B.1})$$

where  $\sigma_{xx}$  is the horizontal normal stress component. The shear stress within the fractured layer varies approximately linear with  $y$  (Fig. B1a). Mechanical equilibrium demands that a gradient in horizontal normal stress,  $d\sigma_x/dx$ , within the layer is balanced by an interfacial shear stress,  $\tau_x$ .

$$\frac{d\sigma_x}{dx} + \frac{\tau_x^{top} - \tau_x^{bot}}{t} = 0 \quad (\text{B.2})$$

The superscripts refer to the shear stress acting on the top and bottom layer interface. If the top and bottom interfacial shear stresses are identical in magnitude, but opposite in sign, then Eq. B.2 can be written as

$$\frac{d\sigma_x}{dx} = -\frac{2\tau_x}{t} \quad (\text{B.3})$$

A positive normal stress gradient hence leads to a negative (counter-clockwise) shear stress along the *upper* interface (Fig. B1a).

We assume that the maximum interfacial shear stress,  $\tau$ , is given by a Coulomb limit

$$|\tau| = \sigma_y \mu, \quad (\text{B.4})$$

where  $\sigma_y$  is the normal stress acting on the interface and  $\mu$  is the interfacial friction coefficient.

## B.2 No-slip solution

Cox (1952) derived a solution that conforms with the boundary conditions outlined above. In the absence of interfacial slip the average layer-parallel normal stress within a fracture-bound block is

$$\sigma_x(x) = E_f e_m \left( 1 - \frac{\cosh(\beta(L-x))}{\cosh(\beta L)} \right) \quad (\text{B.5})$$

where  $\beta$  is the load transfer parameter. For the sake of mathematical brevity the origin ( $x = 0$ ) in Eq. B.5 is located at the left hand fracture. If the shear stress in the matrix decreases linearly in a vertical direction from its maximum value at the interface to zero midway between two fracturing layers (Fig. B1a) then  $\beta$  is (Ji et al., 1998)

$$\beta = \sqrt{\frac{8G_m}{E_f t d}} \quad (\text{B.6})$$

where  $G_m$  is the shear modulus of the matrix. The actual shear stress may decrease non-linearly and various analytical solutions have been postulated to take a non-linear shear stress decay into account (Ji and Saruwatari, 1998, Jain et al., 2007). We prefer, however, to determine the value of  $\beta$  in our models directly as outlined in Appendix C.

The maximum layer-parallel normal stress within the fractured block,  $\sigma_{max}$ , occurs in the centre ( $x = L$ ) and given by

$$\sigma_{max} = E_f e_m (1 - \text{sech}(\beta L)) \quad (\text{B.7})$$

The shear stress acting on the interface,  $\tau_x$ , can be obtained by differentiating Eq. B.5 and substituting the result into Eq. B.3.

$$\tau_x(x) = \frac{t}{2} E_f e_m \beta \frac{\sinh(\beta(L-x))}{\cosh(\beta L)} \quad (\text{B.8})$$

where the absence of the minus sign indicates that Eq. B.8 describes the shear stress distribution along the *lower* interface. The maximum interface shear stress,  $\tau_{max}$ , occurs at the end of the fractured block ( $x = 0$ ) and is

$$\tau_{max} = \frac{t}{2} E_f e_m \beta \frac{\sinh(\beta L)}{\cosh(\beta L)} \quad (\text{B.9})$$

Average normal stress and interfacial shear stress profiles that were calculated using

these solutions are plotted in Fig. B1bi.

If we assume that the average normal stress in the fracturing layer cannot exceed the tensile strength,  $T$ , then a limiting, or *critical half-length*  $L_c$ , below which no fracturing can occur at a particular matrix strain, exists (Lloyd et al., 1982). The critical half-length,  $L_c$ , can then be obtained by replacing  $\sigma_{max}$  in Eq. B.7 with  $T$  and solving for  $L$

$$L_c^{noslip} = \frac{1}{\beta} \operatorname{asech} \left( 1 - \frac{T}{E_f e_m} \right) \quad (\text{B.10})$$

where the superscript *noslip* denotes that this is the critical half-length for a welded interface. For infinite matrix strain Eq. B.10 becomes

$$\lim_{e_m \rightarrow \infty} L_c^{noslip} = 0$$

which is clearly not possible, but sometimes used as an argument against the shear lag model (Bai et al., 2000). However, interfacial slip will occur if the maximum interface shear stress,  $\tau_{max}$ , exceeds the shear strength of the interface,  $\tau$  (Ji et al., 1998, Jain et al., 2007). The matrix strain at which interfacial slip commences can be obtained by substituting the critical half-length for a welded interface (Eq. B.10) as  $L$  into Eq. B.9 and replacing  $\tau_{max}$  with  $\tau$ . Solving for  $e_m$  and simplifying gives

$$e_m^{sliponset} = \frac{4\tau^2 + (T\beta t)^2}{2E_f T(\beta t)^2} \quad (\text{B.11})$$

From this point onwards the interface is comprised of two regions, (I) slip, or plastic, regions near the fractures and (II) a no-slip, or elastic, region in the centre of the fractured block (Fig. B1bii). In the limit, the entire interface will be sliding (Fig. B1biii).

The critical half-length at the onset of slip can be obtained by substituting the matrix strain at the onset of slip given by Eq. B.11 into Eq. B.10 and is

$$L_c^{sliponset} = \frac{1}{\beta} \operatorname{asech} \left( \frac{4\tau^2 - (T\beta t)^2}{4\tau^2 + (T\beta t)^2} \right) \quad (\text{B.12})$$

Eq. B.12 indicates that the interfacial shear strength  $\tau$  must have a certain minimum value (the numerator in the inverse hyperbolic secant term must be  $> 0$ ), otherwise the entire interface will slip as soon as the first fracture appears and no further fracture is possible.

$$\tau > \frac{T\beta t}{2} \quad (\text{B.13})$$

This inequality can alternatively be obtained by the condition that the matrix strain at the onset of fracture must be less than the strain at the onset of interfacial slip (Eq. B.11), i.e.  $e_m^{sliponset} > T/E_f$ .

### B.3 Full-slip solution

If the normal stress acting on the interface,  $\sigma_y$ , remains constant and uniform while slip occurs, then the shear stress acting on the interface is also constant and given by Eq. B.4. As a consequence the gradient of the layer-parallel normal stress within the fracture layer is constant, i.e. the layer-parallel stress profile is a triangle (Eq. B.3; see Fig. B1biii). The normal stress is, however, limited by the tensile strength,  $T$ , so that  $d\sigma_x/dx$  in Eq. B.3 can be replaced by  $T/L$ . The critical half-length of the fractured block, below which no further fracture can occur, is therefore given by

$$L_c^{fullslip} = \frac{Tt}{2\tau} \quad (\text{B.14})$$

Eq. B.14 is known as Price's model in Earth Sciences (Price, 1966, Mandl, 2005) and as Kelly-Tyson equation in Material Sciences (Kelly and Tyson, 1965, Tripathi and Jones, 1998).

### B.4 Partial-slip solution

It is clear that the two models outlined above, i.e. the no-slip and the full-slip solution, are end-member scenarios. The onset of interfacial slip is derived above and given by Eq.



B.11. An increase in extension leads to a progressive increase of the length of the slip region until, in theory, the entire interface is sliding.

Here we use a Piggott model (Piggott, 1978, Huang and Young, 1995, van den Heuvel et al., 1997) where a linear stress build-up (Eq. B.3) in the slip region is immediately followed by an elastic stress build-up according to Cox's shear lag model (Eq. B.5).

$$\sigma_x(x) = \begin{cases} \frac{2\tau}{t}x = gx & 0 \leq x \leq x_t \\ gx_t + (E_f e_m - gx_t) \left( 1 - \frac{\cosh(\beta(L-x))}{\cosh(\beta(L-x_t))} \right) & x_t \leq x \leq L \end{cases} \quad (\text{B.15})$$

where  $x_t$  is the transition point from the slip to no-slip region and  $g$  is the normal stress gradient in the slip region, which is a constant, and used here for brevity. Eq. B.15 is, again, given for the left-hand side of a fracture-bound block with the left-hand fracture located at  $x = 0$ . Notice that Eq. B.15 becomes Cox's solution (Eq. B.5) if  $x_t = 0$  and that the full-slip solution (Eq. B.14) is obtained when  $e_m = \infty$ .

The maximum layer-parallel normal stress occurs at the centre of the bonded region, at  $L$ , and is given by

$$\sigma_{max} = gx_t + (E_f e_m - gx_t)(1 - \text{sech}(\beta(L - x_t))) \quad (\text{B.16})$$

Analogous to the no-slip case, the shear stress acting on the interface,  $\tau_x$ , can be obtained by differentiating Eq. B.15 and substituting the result into Eq. B.3.

$$\tau_x(x) = \begin{cases} \tau & 0 \leq x \leq x_t \\ \frac{t}{2}(E_f e_m - gx_t)\beta \frac{\sinh(\beta(L-x))}{\cosh(\beta(L-x_t))} & x_t \leq x \leq L \end{cases} \quad (\text{B.17})$$

The maximum interfacial shear stress,  $\tau_{max}$ , occurs at the end of the bonded region ( $x = x_t$ ) and is given by

$$\tau_{max} = \frac{t}{2}(E_f e_m - g x_t) \beta \frac{\sinh(\beta(L - x_t))}{\cosh(\beta(L - x_t))} \quad (\text{B.18})$$

538 The critical half-length is determined by limiting the maximum normal stress given  
539 by Eq. B.16 by the tensile strength  $T$  and solving for  $L$ .

$$L_c^{partialslip} = x_t + \frac{1}{\beta} \operatorname{asech} \left( \frac{T - E_f e_m}{g x_t - E_f e_m} \right) \quad (\text{B.19})$$

540 For a *cohesionless* interface (Eq. B.4) the unknown  $x_t$  can be evaluated by assuming  
541 stress continuity at the transition point, for which the maximum interface shear stress (Eq.  
542 B.18) is equal to the shear strength  $\tau$ . For a cohesive interface stress continuity cannot  
543 be justified and an interfacial shear stress jump and an associated increase of the average  
544 layer-parallel normal stress gradient occurs (Huang and Young, 1995, van den Heuvel  
545 et al., 1997). In the present study, however, the effect of cohesion is not investigated and  
546 we therefore assume that the interfacial shear strength is provided by friction only.

547 Taking  $\tau$  as  $\tau_{max}$  in Eq. B.18 and substituting  $L$ , as given by Eq. B.19, gives after  
548 rearrangement.

$$2\tau - \beta t \sqrt{(g x_t - T)(g x_t + T - 2E_f e_m)} = 0 \quad (\text{B.20})$$

549 Unfortunately a closed form solution for Eq. B.20 does not exist and therefore  $x_t$  has  
550 to be determined numerically. The result can then be substituted into Eq. B.19 and the  
551 critical half-length for the partial-slip case can be obtained. Average normal stress and  
552 interfacial shear stress profiles that were calculated using these solutions are plotted in  
553 Fig. B1bii.

## 554 B.5 Implementation

555 The critical half-length,  $L_c$  and, if slip occurs, the length of the slip region,  $x_t$ , can be  
556 calculated as a function of matrix strain using a simple computer program (a MATLAB  
557 script can be obtained upon request from the corresponding author). The input param-

ters are the layer thicknesses,  $t$  and  $d$ , the elastic properties,  $E_f$  and  $G_m$ , the layer tensile and interface shear strengths,  $T$  and  $\tau$ , respectively, and the matrix strain,  $e_m$ . The algorithm is structured as follows:

If  $E_f e_m > T$  And  $\tau > T\beta t/2$  (Eq. B.13) Then

If  $e_m \leq e_m^{slip\ onset}$  (Eq. B.11) Then

Calculate  $L_c^{noslip}$  (Eq. B.10),  $x_t = 0$

Else

Determine  $x_t$  numerically (Eq. B.20) and calculate  $L_c^{partialslip}$  (Eq. B.19)

EndIf

EndIf

The first if-statement checks (i) whether the strain is high enough to exceed the tensile strength of the layer and (ii) whether the interfacial shear strength is high enough. The second if-statement checks whether the strain is less than the onset of interfacial slip or not. If no-slip occurs, then the no-slip solution is used, otherwise the partial-slip solution is used for calculating  $L_c$  and  $x_t$ .

A plot of  $L_c$  and  $x_t$  vs.  $e_m$  is shown in Fig. B1c. As expected, the critical-half-length decreases with increasing strain and asymptotically approaches the full-slip solution. The length of the slip region gradually increases and eventually becomes equal to the full-slip half-length. If interfacial slip were inhibited, then  $L_c$  asymptotically approaches 0.

## Appendix C Fitting shear lag model to numerical modelling results

An approximation of the average stress, as given by Eq. B.1, within the particle model is obtained by interpolating the horizontal particle stress components,  $\sigma_{xx}^p$ , on a square-grid with a spacing  $\Delta x = \Delta y = 0.0025$  and applying Simpson's rule

$$\sigma_x(x) \cong \alpha \frac{1}{t} \sum_{n=0}^N \sigma_{xx}^p \left( y_0 - \frac{t}{2} + \frac{\Delta y}{2} + \Delta y n \right), \quad \text{where } N = \frac{t}{\Delta y} - 1 \quad (\text{C.1})$$

where  $\alpha$  is the fraction of area occupied by particles ( $\alpha = 0.84$  in our models).

For each fracture-bound block a shear lag model with partial slip (Section B.4) is fitted to the approximate average stress data to obtain an estimate for the load transfer parameter  $\beta$  (Fig. 3). First the magnitude and location of the maximum horizontal normal stress  $\sigma_{max}$  is calculated by fitting a  $2^{nd}$ -order polynomial to six consecutive points. The stress profiles are often asymmetric, hence the best-fit  $\beta$ -value is calculated for the right and left hand side separately. Each side has a length of  $L$ , which is comprised of a slip-region with length  $x_t$  and a no-slip region with length  $mL$ , where  $m = 1 - x_t/L$ .

Again, we assume stress continuity from the slip to no-slip region, so that the maximum shear stress at the ends of the no-slip region  $\tau_{max}$  is equal to the interface shear strength  $\tau$ . Using  $2\tau/t$  instead of  $g$  and  $mL$  instead of  $(L - x_t)$  in Eq. B.18 and solving for  $x_t$  gives

$$x_t = \frac{E_f e_m t}{2\tau} - \frac{\cosh(mL\beta)}{\beta \sinh(mL\beta)} \quad (C.2)$$

Substitution of Eq. C.2 into Eq. B.16 and using again  $mL$  instead of  $(L - x_t)$  gives

$$E_f e_m - \frac{2\tau}{t\beta} \cosh(mL\beta) \frac{\operatorname{sech}(mL\beta)}{\sinh(mL\beta)} - \sigma_{max} = 0 \quad (C.3)$$

The  $\beta$ -value can be determined numerically from Eq. C.3 and  $x_t$  can then be calculated using Eq. C.2. The best-fit  $\beta$ -value is obtained by iteratively varying  $m$  in the range of 0.0 to 1.0 and minimising the sum-of-squares  $\sigma_x$  differences between model profile and shear lag equation (Eq. B.15).

It is important to note that the condition  $\tau_{max} = \tau$  can only be justified if interfacial slip actually occurs (prior to interfacial slip  $\tau_{max} < \tau$ ). In addition  $\beta$  is poorly constrained when slip occurs over almost the entire length of a fracture-bound block (e.g. at fracture saturation). Hence the best-fit  $\beta$ -value used for predicting the fracture and slip evolution (Fig. 5) is the arithmetic mean of all best-fit  $\beta$ -values where  $0.1 < x_t/L < 0.9$ . The best-fit  $\beta$ -values for all four models are provided in Fig 5a.

## References

- Adda-Bedia, M., Amar, M. B., 2001. Fracture spacing in layered materials. *Physical Review Letters* 86, 5703–5706.
- Altus, E., Ishai, O., 1986. Transverse cracking and delamination interaction in the failure process of composite laminates. *Composites Science and Technology* 26, 59–77.
- Bai, T., Pollard, D. D., 2000a. Closely spaced fractures in layered rocks: initiation mechanism and propagation kinematics. *Journal of Structural Geology* 22, 1409–1425.
- Bai, T., Pollard, D. D., 2000b. Fracture spacing in layered rocks: a new explanation based on the stress transition. *Journal of Structural Geology* 22, 43–57.
- Bai, T., Pollard, D. D., Gao, H., 2000. Explanation for fracture spacing in layered materials. *Nature* 403, 753–756.
- Berthelot, J.-M., 2003. Transverse cracking and delamination in cross-ply glass-fiber and carbon-fiber reinforced plastic laminates: Static and fatigue loading. *Applied Mechanics Reviews* 56, 111–147.
- Berthelot, J.-M., Leblond, P., El Mahi, A., Le Corre, J. F., 1996. Transverse cracking of cross-ply laminates: Part 1. Analysis. *Composites Part A: Applied Science and Manufacturing* 27, 989–1001.
- Bourne, S. J., 2003. Contrast of elastic properties between rock layers as a mechanism for the initiation and orientation of tensile failure under uniform remote compression. *Journal of Geophysical Research* 108, (B8)2395.
- Byerlee, J., 1978. Friction of rocks. *Pure and Applied Geophysics* 116, 615–626.
- Cooke, M. L., Underwood, C. A., 2001. Fracture termination and step-over at bedding interfaces due to frictional slip and interface opening. *Journal of Structural Geology* 23, 223–238.
- Cox, H. L., 1952. The elasticity and strength of paper and other fibrous materials. *British Journal of Applied Physics* 3, 72–79.
- Dharani, L. R., Wei, J., Ji, F. S., Zhao, J. H., 2003. Saturation of transverse cracking with delamination in polymer cross-ply composite laminates. *International Journal of Damage Mechanics* 12, 89–113.
- Garrett, K. W., Bailey, J. E., 1977. Multiple transverse fracture in 90° cross-ply laminates of a glass fibre-reinforced polyester. *Journal of Materials Science* 12, 157–168.
- Gillespie, P. A., Walsh, J. J., Watterson, J., Bonson, C. G., Manzocchi, T., 2001. Scaling relationships of joint and vein arrays from The Burren, Co. Clare, Ireland. *Journal of Structural Geology* 23, 183–201.
- Groves, S. E., Harris, C. E., Highsmith, A. L., Allen, D. H., Norvell, R. G., 1987. An experimental and analytical treatment of matrix cracking in cross-ply laminates. *Experimental Mechanics* 27, 73–79.
- Hobbs, D. W., 1967. The formation of tension joints in sedimentary rocks: an explanation. *Geological Magazine* 104, 550–556.
- Hu, S., Bark, J. S., Nairn, J. A., 1993. On the phenomenon of curved microcracks in  $[(S)/90_n]_s$  laminates: their shapes, initiation angles and locations. *Composites Science and Technology* 47, 321–329.
- Huang, Q., Angelier, J., 1989. Fracture spacing and its relation to bed thickness. *Geological Magazine* 126, 355–362.
- Huang, Y., Young, R. J., 1995. Interfacial behaviour in high temperature cured carbon fibre/epoxy resin model composite. *Composites* 26, 541–550.

- Itasca Consulting Group, Inc., 2008. PFC2D (Particle Flow Code in 2 Dimensions), Version 4.0. Minneapolis, MN.
- Iyer, K., Podladchikov, Y. Y., 2009. Transformation-induced jointing as a gauge for interfacial slip and rock strength. *Earth and Planetary Science Letters* 280, 159–166.
- Jain, A., Guzina, B. B., Voller, V. R., 2007. Effects of overburden on joint spacing in layered rocks. *Journal of Structural Geology* 29, 288–297.
- Ji, S., Saruwatari, K., 1998. A revised model for the relationship between joint spacing and layer thickness. *Journal of Structural Geology* 20, 1495–1508.
- Ji, S., Zhu, Z., Wang, Z., 1998. Relationship between joint spacing and bed thickness in sedimentary rocks: effects of interbed slip. *Geological Magazine* 135, 637–655.
- Kelly, A., Tyson, W. R., 1965. Tensile properties of fiber-reinforced metals: copper/tungsten and copper/molibdenum. *Journal of the Mechanics and Physics of Solids* 13, 329–350.
- Korach, C. S., Keer, L. M., 2002. Stresses between 3D fractures in infinite and layered elastic solids. *Engineering Fracture Mechanics* 69, 1815–1825.
- Ladeira, F. L., Price, N. J., 1981. Relationship between fracture spacing and bed thickness. *Journal of Structural Geology* 3, 179–183.
- Li, Y., Yang, C., 2007. On fracture saturation in layered rocks. *International Journal of Rock Mechanics and Mining Sciences* 44, 936–941.
- Lloyd, G. E., Ferguson, C. C., Reading, K., 1982. A stress-transfer model for the development of extension fracture boudinage. *Journal of Structural Geology* 4, 355–372.
- Lockner, D. A., 1995. Rock failure. In: Ahrens, T. J. (Ed.), *Rock Physics & Phase Relations. A Handbook of Physcial Constants*. AGU Reference Shelf 3. American Geophysical Union, Washington DC, pp. 127–147.
- Mandal, N., Deba, S. K., Khan, D., 1994. Evidence for a non-linear relationship between fracture spacing and layer thickness. *Journal of Structural Geology* 16, 1275–1281.
- Manders, P. T., Chou, T.-S., Jones, F. R., Rock, J. W., 1983. Statistical analysis of multiple fracture in 00°/90°/0° glass fibre/epoxy resin laminates. *Journal of Materials Science* 18, 2876–2889.
- Mandl, G., 2005. *Rock Joints: The Mechanical Genesis*. Springer-Verlag, Heidelberg.
- Mas Ivars, D., Potyondy, D. O., Pierce, M., Cundall, P. A., 2008. The smooth-joint contact model. In: Schrefler, B., Perego, U. (Eds.), *Proceedings of WCCM8 - ECCOMAS 2008, (8th World Congress on Computational Mechanics/5th European Congress on Computational Methods in Applied Sciences and Engineering)*.
- Nairn, J. A., 2000. Matrix microcracking in composites. In: Talreja, R., Manson, J.-A. E. (Eds.), *Comprehensive Composite Materials Vol. 2: Polymer Matrix Composites*. Elsevier Science, Amsterdam, pp. 403–432.
- Narr, W., Suppe, J., 1991. Joint spacing in sedimentary rocks. *Journal of Structural Geology* 13, 1037–1048.
- Ohsawa, T., Nakayama, N., Miwa, M., Hasegawa, A., 1978. Temperature dependence of critical fiber length for glass fiber-reinforced thermosetting resins. *Journal of Applied Polymer Science* 22, 3203–3212.

- Olson, J. E., 2004. Predicting fracture swarms - the influence of subcritical crack growth and the crack-tip process zone on joint spacing in rock. In: Cosgrove, J. W., Engelder, T. (Eds.), *The Initiation, Propagation, and Arrest of Joints and Other Fractures*, Geol. Soc. Lond. Spec. Publ. 231. Geological Society, London, pp. 73–88.
- Parvizi, A., Bailey, J. E., 1978. On multiple transverse cracking in glass fibre epoxy cross-ply laminates. *Journal of Materials Science* 13, 2131–2136.
- Piggott, M. R., 1978. Expressions governing stress-strain curves in short fibre reinforced polymers. *Journal of Materials Science* 13, 1709–1716.
- Piggott, M. R., 1997. Why interface testing by single-fibre methods can be misleading. *Composites Science and Technology* 57, 965–974.
- Potyondy, D. O., Cundall, P. A., 2004. A bonded-particle model for rock. *International Journal of Rock Mechanics and Mining Sciences* 41, 1329–1364.
- Price, N. J., 1966. *Fault and Joint Development in Brittle and Semi-Brittle Rock*. Pergamon Press Ltd., Oxford.
- Ramsey, J. M., Chester, F. M., 2004. Hybrid fracture and the transition from extension fracture to shear fracture. *Nature* 428, 63–66.
- Sagy, A., Reches, Z., 2006. Joint intensity in layered rocks: The unsaturated, saturated, supersaturated and clustered classes. *Israel Journal of Earth Sciences* 55, 33–42.
- Savalli, L., Engelder, T., 2005. Mechanisms controlling rupture shape during subcritical growth of joints in layered rocks. *Geological Society of America Bulletin* 117, 436–449.
- Schoeppner, G. A., Pagano, N. J., 1999. 3-D thermoelastic moduli and saturation crack density for cross-ply laminates with transverse cracks. *International Journal of Damage Mechanics* 8, 273–309.
- Schöpfer, M. P. J., Abe, S., Childs, C., Walsh, J. J., 2009. The impact of porosity and crack density on the elasticity, strength and friction of cohesive granular materials: Insights from DEM modelling. *International Journal of Rock Mechanics and Mining Sciences* 46, 250–261.
- Schöpfer, M. P. J., Childs, C., Walsh, J. J., 2007. Two-dimensional distinct element modeling of the structure and growth of normal faults in multilayer sequences: 2. Impact of confining pressure and strength contrast on fault zone geometry and growth. *Journal of Geophysical Research* 112, B10404.
- Sibson, R. H., 1998. Brittle failure mode plots for compressional and extensional tectonic regimes. *Journal of Structural Geology* 20, 655–660.
- Tang, C. A., Liang, Z. Z., Zhang, Y. B., Chang, X., Tao, X., Wang, D. G., Zhang, J. X., Liu, J. S., Zhu, W. C., Elsworth, D., 2008. Fracture spacing in layered materials: a new explanation based on two-dimensional failure process modeling. *American Journal of Science* 308, 49–72.
- Tripathi, D., Jones, F. R., 1998. Single fibre fragmentation test for assessing adhesion in fibre reinforced composites. *Journal of Materials Science* 33, 1–16.
- van den Heuvel, P. W. J., Peijs, T., Young, R. J., 1997. Failure phenomena in two-dimensional multifibre microcomposites: 2. A raman spectroscopic study of the influence of inter-fibre spacing on stress concentrations. *Composites Science and Technology* 57, 899–911.
- Wu, H., Pollard, D. D., 1995. An experimental study of the relationship between joint spacing and layer thickness. *Journal of Structural Geology* 17, 887–905.

## Tables

$\mu$	$e_p$	$\sigma_p$ (MPa)	$E_p$ (GPa)	$E_f$ (GPa)	$T$ (MPa)
0.2	0.0000290	-1.65	56.95	36.18	6.68
0.3	0.0000298	-1.66	55.79	35.35	6.38
0.5	0.0000293	-1.68	57.30	36.47	6.25
0.8	0.0000295	-1.66	56.11	35.42	6.62
<b>Mean</b>	0.0000294	-1.66	56.54	35.85	6.48

**Table A1:** Material and model parameters obtained from measurement circles (see Fig. A1) for four models with different interfacial friction coefficients,  $\mu$ .



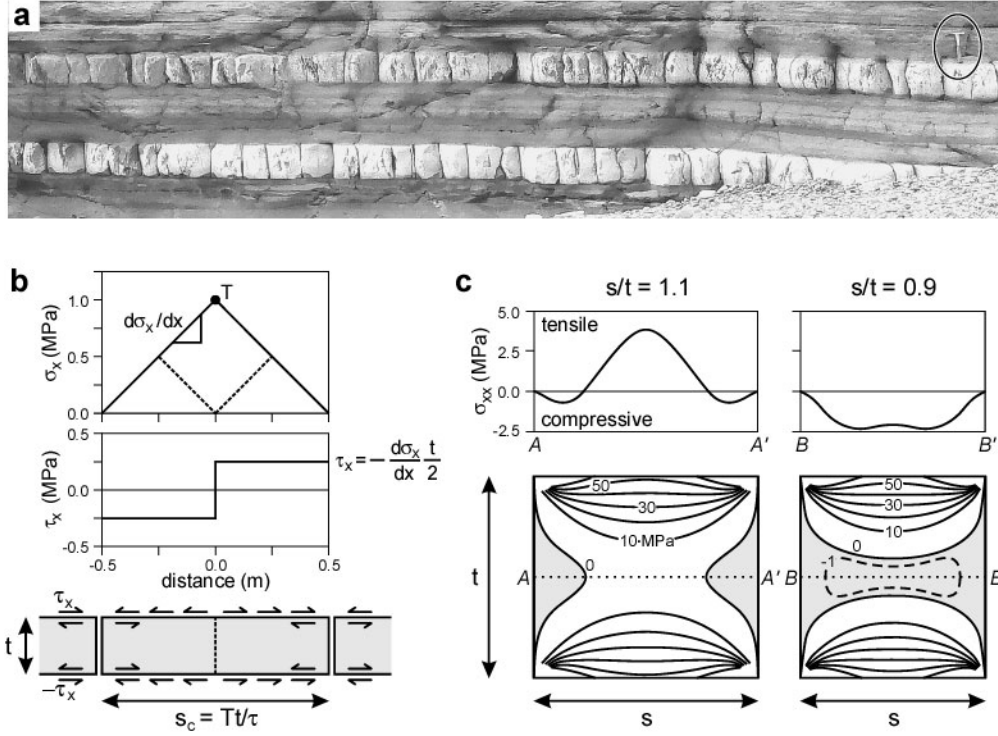


**Figure 1:** Natural example of layer-confined opening fractures and illustrations of theories for fracture saturation. **a**, Field example of rock joints (opening fractures) developed within limestone beds (pale) embedded in mudrocks (grey) exposed in Lillstock Bay, Somerset, UK. Rock hammer (circled) is 0.29 m long. **b**, *Full-slip*, or frictional coupling, model (Kelly and Tyson, 1965, Price, 1966). A constant interfacial shear stress  $\tau_x$  is balanced by a layer-parallel normal stress gradient  $d\sigma_x/dx$ . The normal stress is limited by the layer tensile strength  $T$  which leads to a critical fracture spacing  $s_c$  below which no further fracture can occur. The dashed lines indicate that the minimum fracture spacing is  $0.5s_c$ . **c**, *Compressive stress criterion* (Dharani et al., 2003), or *stress-transition theory* (Bai et al., 2000, Bai and Pollard, 2000b). If no interfacial slip occurs, a region of compressive layer-parallel normal stress  $\sigma_{xx}$  (grey areas) that extends across the central area of the fracture-bound block develops at a fracture spacing to thickness ratio ( $s/t$ ) of  $\sim 1.0$  (modified after Bai and Pollard, 2000a,b)

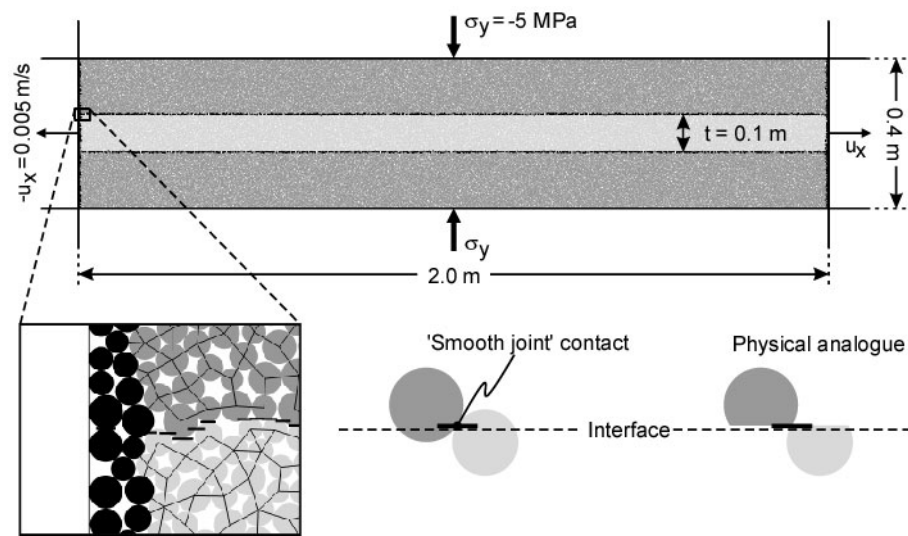


**Figure 2:** Numerical model and its boundary conditions used for modelling rock joints. Dark and light grey particles comprise the matrix and central layer, respectively, and black particles are lateral boundaries to which a horizontal velocity is applied. Black lines joining particle centres are bonds and bold horizontal lines at the layer interface are 'smooth-joint' contacts (see inset).  $\sigma_y$ , vertical applied boundary stress.  $u_x$ , horizontal applied boundary velocity.  $t$ , thickness of central layer.

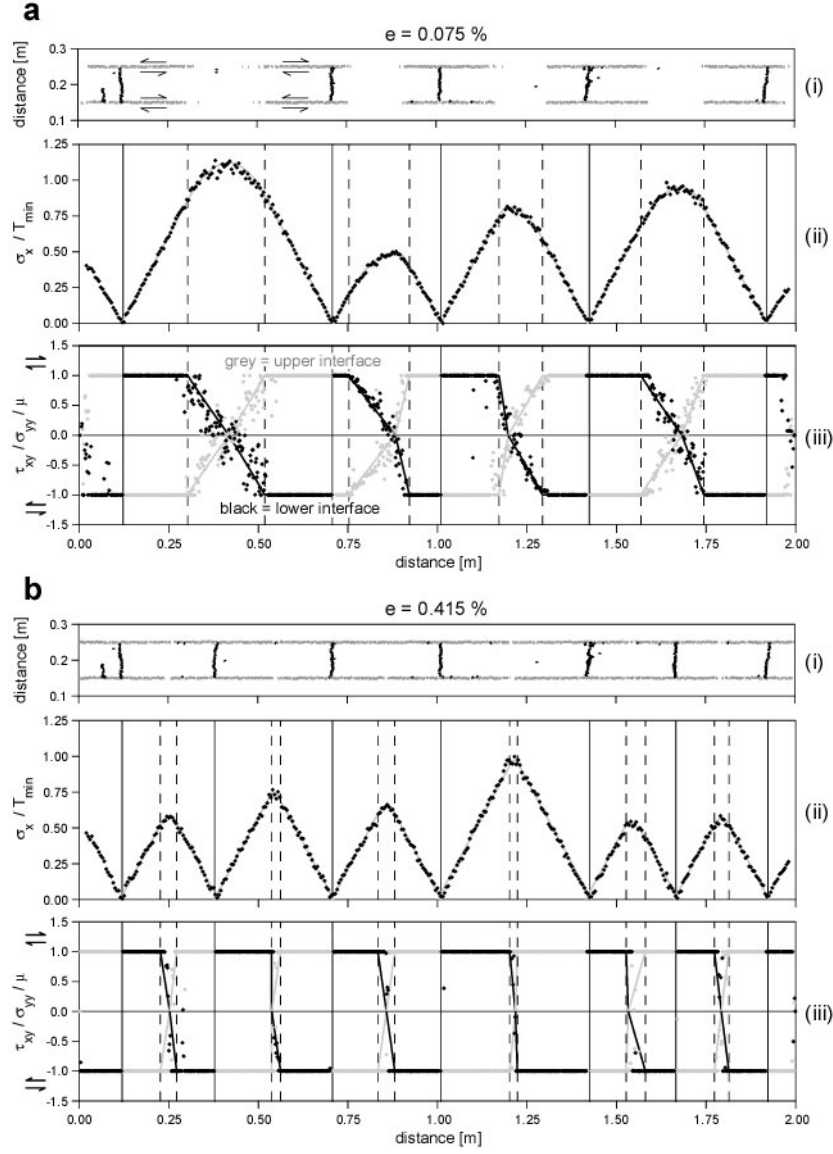


**Figure 3:** Average layer-parallel normal stress and interfacial shear stress distribution in discontinuum model with low interface friction coefficient ( $\mu = 0.3$ ) at ( **a** )  $e = 0.075\%$  and ( **b** )  $e = 0.415\%$ . (i) Locations of broken bonds (black) and sliding 'smooth-joint' contacts (grey). The sense of shear is indicated with half arrows for one fracture-bound block. (ii) Average horizontal, or layer-parallel, stress in fracture layer ( $\sigma_x$ ) normalised by the minimum tensile strength ( $T_{min}$ ). Black dots are model stress data and grey lines are best-fit shear lag model profiles. (iii) Interface shear stress to normal stress ratio ( $\tau_{xy}/\sigma_{yy}$ ) normalised by interface friction coefficient ( $\mu$ ). Black and grey dots are 'smooth-joint' contact stress data of the lower and upper interface, respectively. Solid lines are best-fit shear lag model solutions. Positions of fractures and slip to no-slip regions are indicated with vertical solid and dashed lines, respectively. See Appendix C for details regarding the best-fit shear lag model. Animations of graphical representation for this and a selection of other models are provided as an electronic supplement.

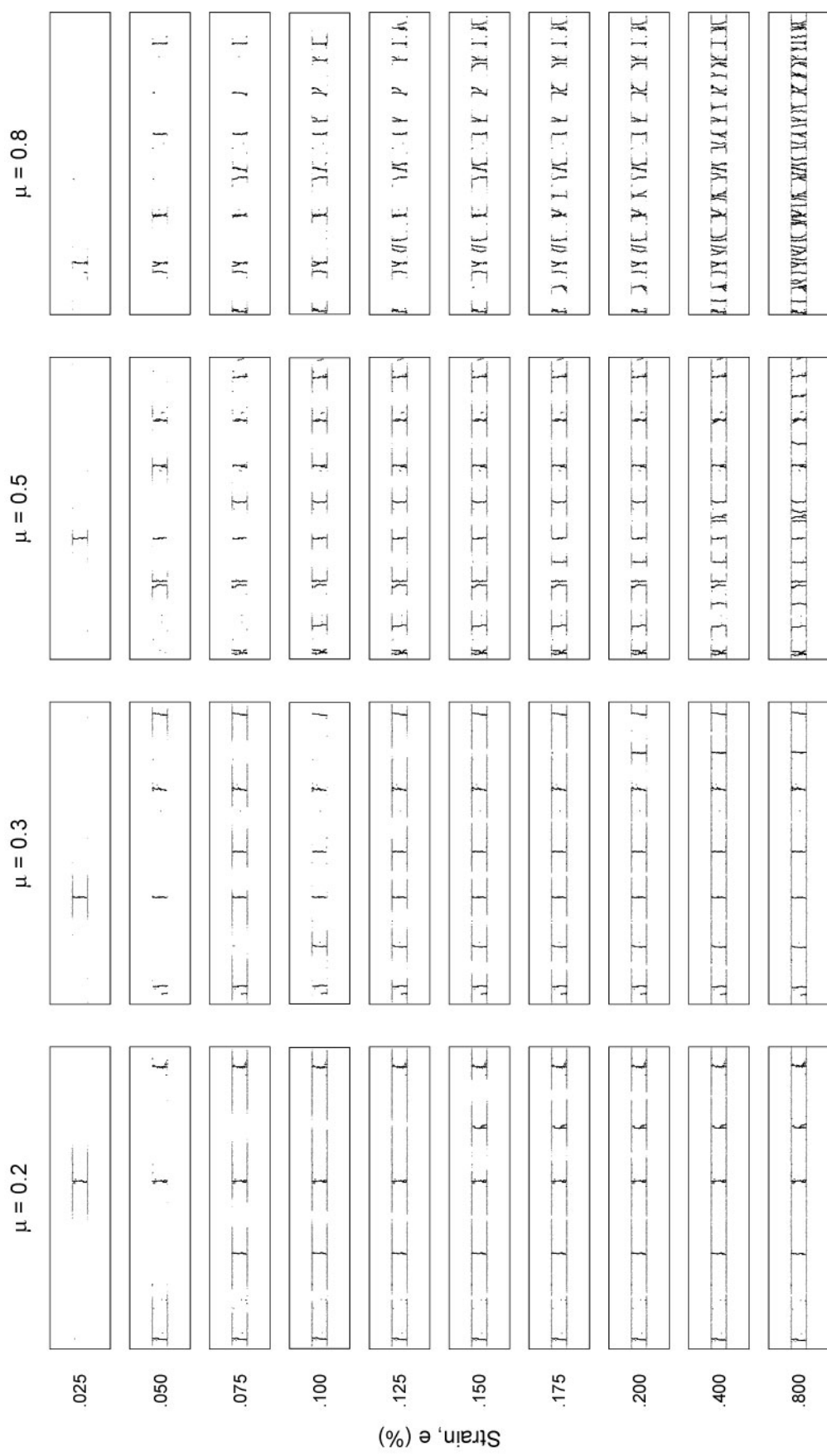


**Figure 4:** Locations of broken bonds (black) and sliding 'smooth-joint' contacts (grey) at various stages of strain.  $\mu$  is the interfacial friction coefficient. The frames are 2.0 m wide and 0.4 m high.

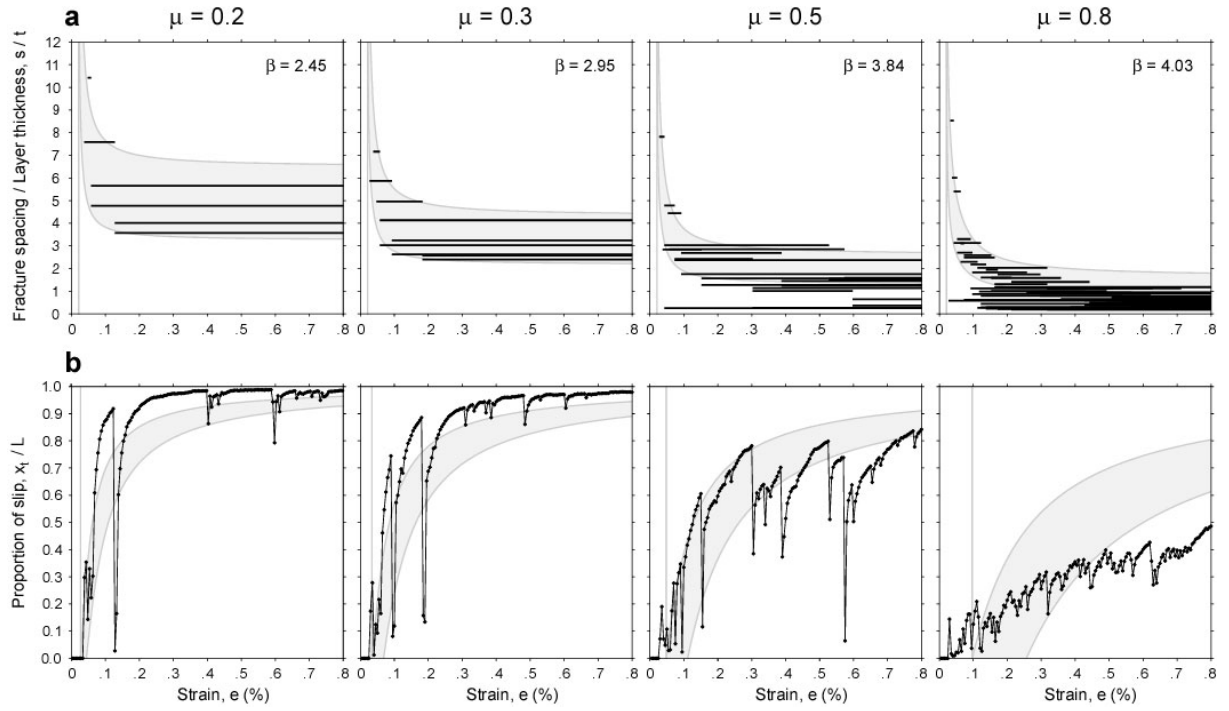


**Figure 5:** Plots of (a) fracture spacing to layer thickness ratios (black horizontal lines) and (b) average proportions of interfacial slip (black lines with dots) vs. layer parallel strain ( $e$ ).  $\mu$  is the interfacial friction coefficient. The start of each horizontal line on the graphs in (a) represents the formation of a fracture bound block within the model; the termination of one line coincides with the formation of two new ones. The grey areas are the ranges predicted by a comparable shear-lag model (see Appendix B and Appendix C). The average best-fit load transfer parameter  $\beta$  is given for each model in (a).

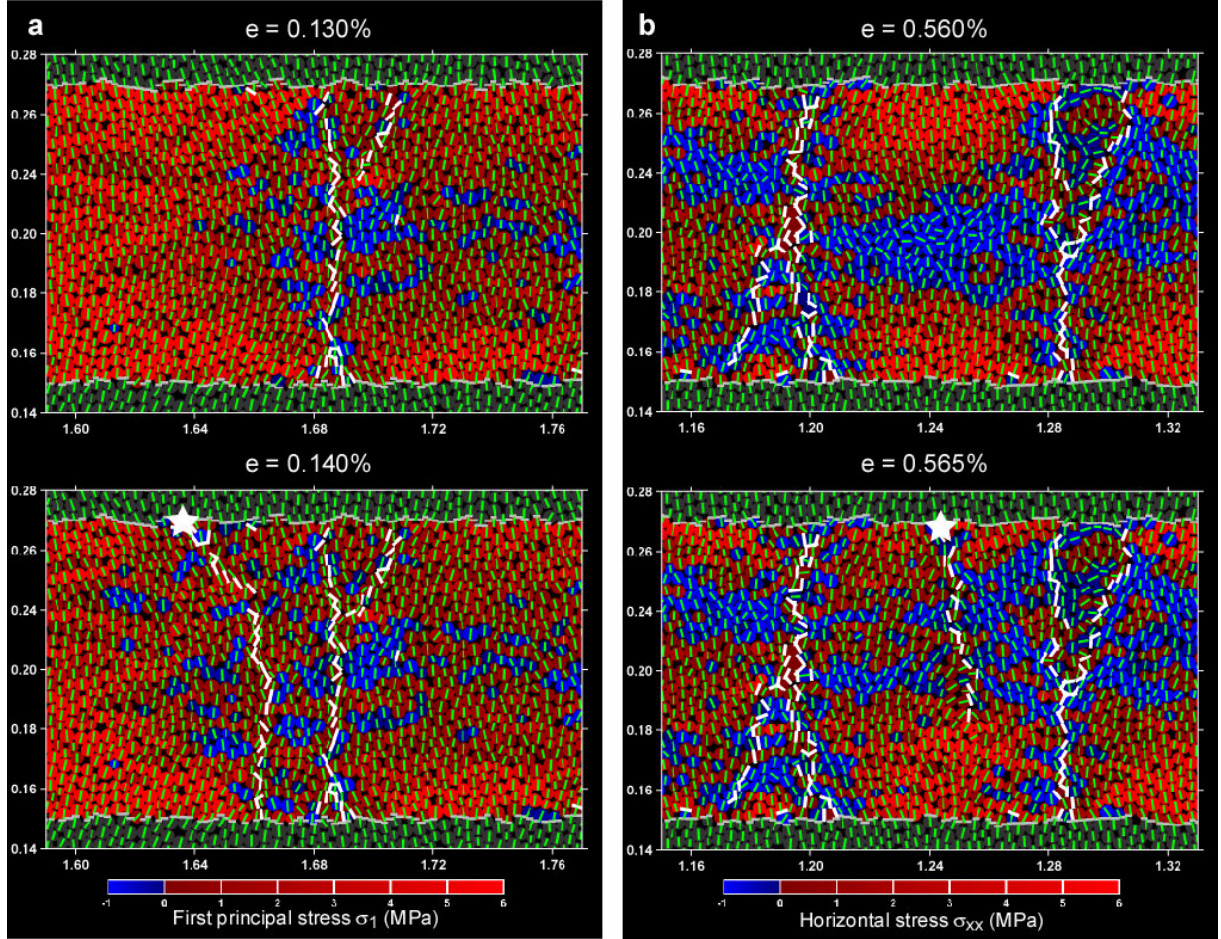


**Figure 6:** Details of 2-D stress distribution within the high interfacial friction ( $\mu = 0.8$ ) model. **a**, Development of a curved fracture (Groves et al., 1987, Hu et al., 1993) adjacent to an existing straight fracture within a fracture-bound block with a spacing to thickness ratio of  $\sim 1.9$ . **b**, Development of an infill fracture (Bai and Pollard, 2000a) within a fracture-bound block with a spacing to thickness ratio of  $\sim 0.9$ . The infill fracture propagates again at  $e = 0.62\%$  to form a through-going fracture (not shown). Particles within the central layer are coloured according to their least compressive stress ( $\sigma_1$ ) in **(a)** and according to horizontal normal stress component ( $\sigma_{xx}$ ) in **(b)**. Matrix particles are dark grey for clarity. Green lines show direction of minimum, i.e. greatest compressive, principal stress. White and grey lines are locations of broken bonds and ‘smooth joint’ contacts, respectively. Stars are fracture nucleation points.  $e$ , model strain.

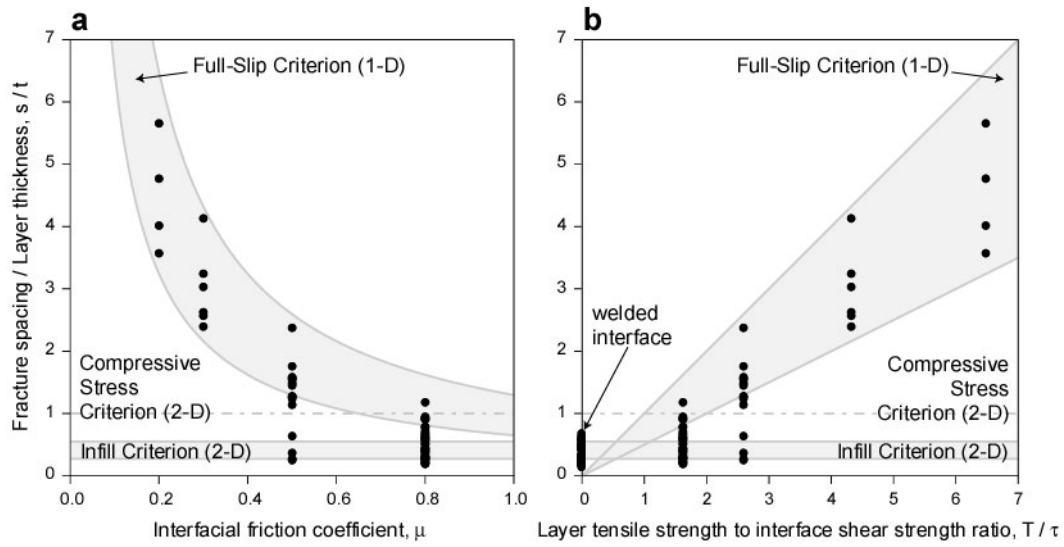


**Figure 7:** Fracture spacing results at a 'fracture-saturated' model strain of  $e = 0.8\%$ . Fracture spacing to layer thickness ratio ( $s/t$ ) is plotted against (a) interfacial friction coefficient  $\mu$  and (b) layer tensile strength to interface shear strength ratio  $T/\tau$ . Fracture spacing for a model with a welded interface (i.e. infinite interfacial shear strength) is plotted in (b) only. The grey areas are the ranges predicted by the full-slip (Kelly and Tyson, 1965, Price, 1966) and fracture infill criterion (Bai and Pollard, 2000a). The grey dashed horizontal line at  $s/t = 1$  is the theoretical fracture spacing when a central layer-parallel compressive normal stress develops (compressive stress criterion; Bai and Pollard, 2000b).

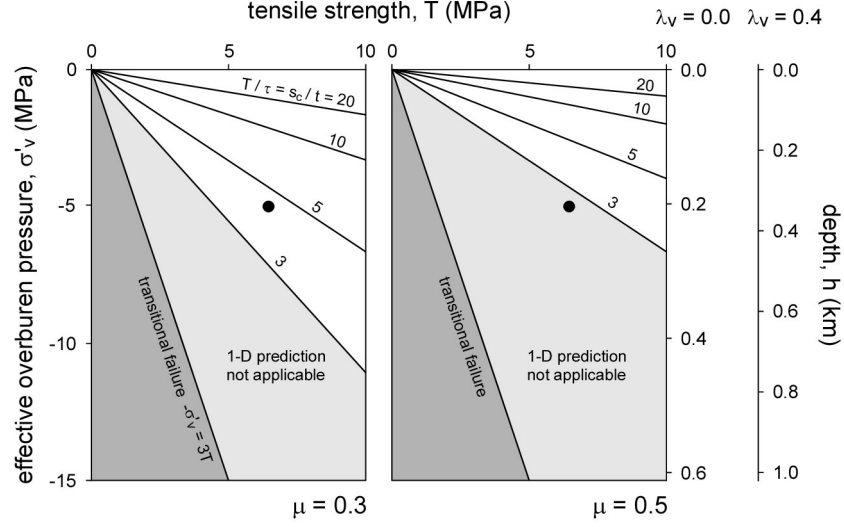


**Figure 8:** Tensile strength vs effective overburden pressure graphs for interfacial friction coefficients  $\mu = 0.3$  and  $0.5$  illustrating (i) layer tensile to interface shear strength ( $T/\tau$ ) contours (which are equivalent to the ratio of maximum, or critical, fracture spacing to layer thickness under full-slip conditions,  $s_c/t$ ; Fig. 1b), (ii) regimes for which our discontinuum models suggest that 1-D full-slip predictions are not applicable ( $T/\tau \lesssim 3$ ; see Fig. 7), and (iii) the transition from pure opening mode fracturing to hybrid extensional-shear fractures, which according to the 2-D Griffith criterion occurs when  $-\sigma'_v > 3T$  (e.g. Sibson, 1998). The effective overburden pressure is  $\sigma'_v = \sigma_v(1 - \lambda_v)$ , with  $\lambda_v = p_f/\sigma_v$  being the ratio of pore fluid pressure  $p_f$  to vertical stress  $\sigma_v$ . Two depth scales are given, one for lithostatic conditions ( $\lambda_v = 0.0$ ) and one where pore water is present and under normal hydrostatic conditions ( $\lambda_v = 0.4$ ). The dots in each graph illustrate the tensile strength and overburden pressure of our discontinuum models. These graphs are strictly speaking only valid for systems with cohesionless interfaces subjected to layer parallel extension.



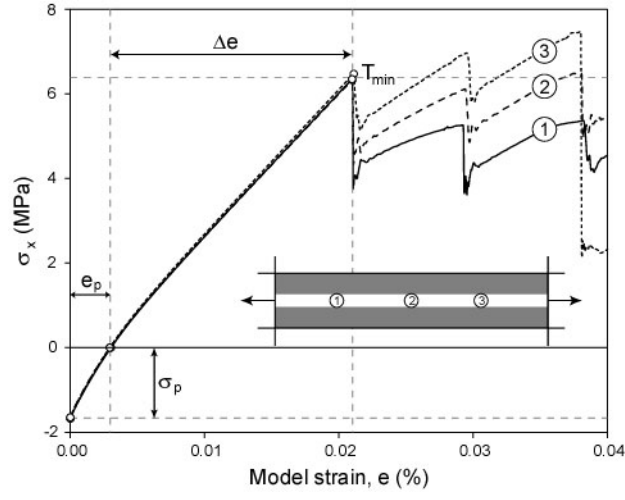


**Figure A1:** Plot of average horizontal stress within three measurement circles (see inset) vs model strain (for the model with  $\mu = 0.3$ ). After uniaxial model confinement a pre-stress,  $\sigma_p$  exists. The strain at which the horizontal stress within the central layer becomes zero is the pre-strain  $e_p$ .  $T_{min}$  is the minimum tensile layer strength and  $\Delta e$  is the strain difference used for calculating the layer secant Young's modulus, i.e.  $E_f = T_{min}/\Delta e$ .

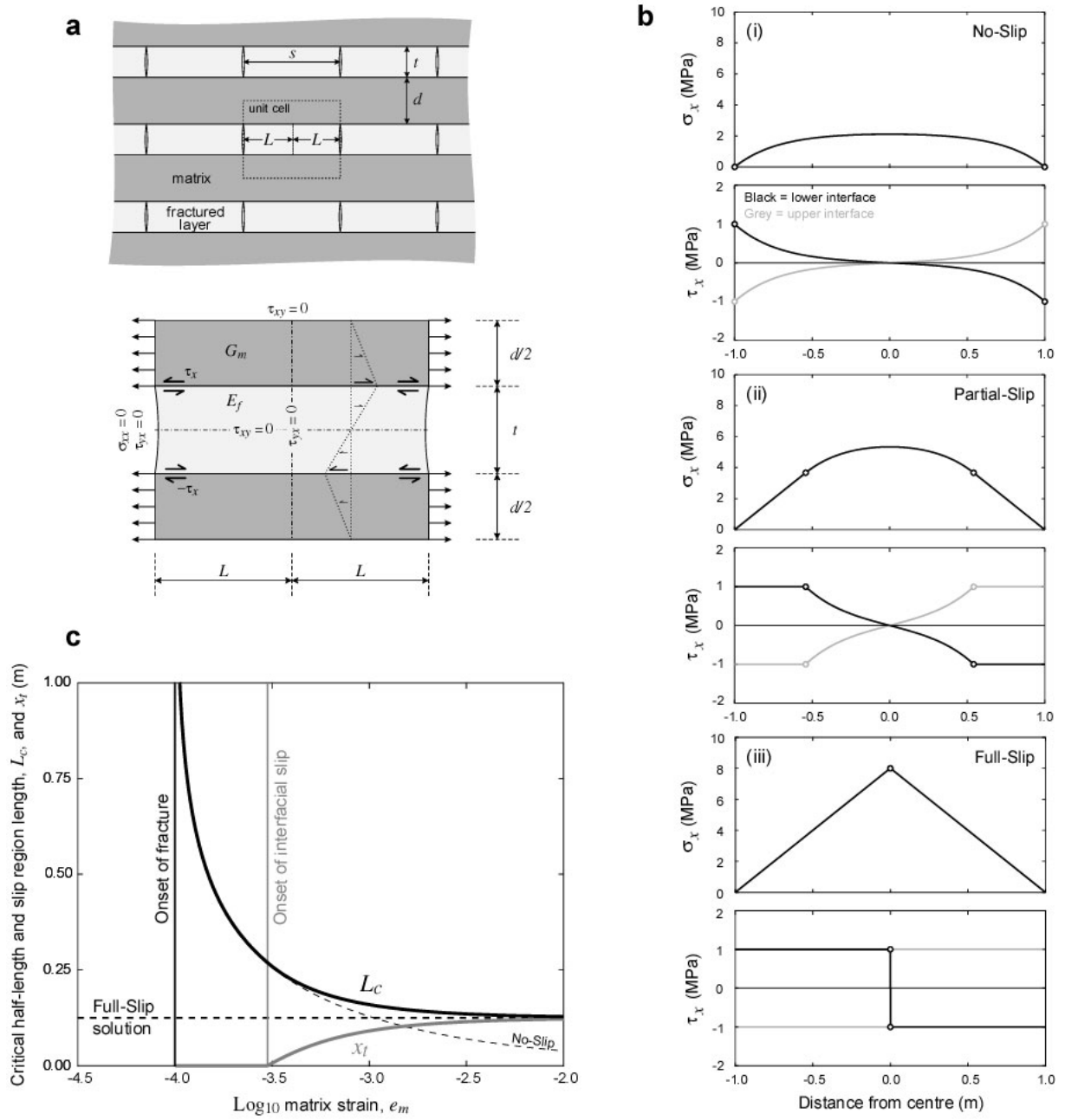


**Figure B1:** 1-D shear lag model used for predicting fracture and interfacial slip evolution in discontinuum models. **a**, Periodically layered sequence comprised of fractured layers with thickness  $t$  interbedded with unfractured matrix layers of thickness  $d$ . The spacing of the fractures is  $s$ , but due to the symmetry of the problem the half-length  $L$  is used. The boundary conditions acting on a 'unit cell' are also shown. **b**, Average horizontal normal stress,  $\sigma_x$ , and interfacial shear stress,  $\tau_x$ , profiles at different matrix strains,  $e_m$ . The dots indicate the transition points from the slip to no-slip region. (i), No-slip solution, just at the onset of slip ( $e_m = 0.000224$  according to Eq. B.11) (ii) Partial-slip solution ( $e_m = 0.0006$ ). (iii) Full-slip solution ( $e_m = \infty$ ). **c**, Plot of critical half-length,  $L_c$  (black curve), and length of slip region,  $x_t$  (grey curve), vs  $\log_{10}$  matrix strain,  $e_m$ . The onset of fracture and the onset of interfacial slip are indicated as vertical lines. The full-slip solution (Eq. B.14) is plotted as horizontal dashed line. The no-slip solution (Eq. B.10) is plotted as thin dashed line for comparison. The parameters used for obtaining the results in (b) and (c) are:  $t = d = 0.25$  m,  $E_f = 10$  GPa,  $G_m = 1$  GPa,  $\tau = 1$  MPa. The  $\beta$ -value is calculated using Eq. B.6. In (b) the half length  $L = 1$  m is kept constant, whereas in (c) the tensile strength  $T = 1$  MPa is constant.